Fractal Grid Generated Turbulence - A Bridge to Practical Combustion Applications

F Hampp and R P Lindstedt‡

Department of Mechanical Engineering, Imperial College, London, SW7 2AZ, UK

E-mail: `p.lindstedt@imperial.ac.uk`

Abstract.
Practical applications typically feature high turbulent Reynolds numbers and, increasingly, low Damköhler numbers leading to distributed combustion. Such conditions are difficult to achieve on a laboratory scale that permits detailed experimental investigations. The aerodynamically stabilised turbulent opposed jet flame configuration is a case point - an exceptionally flexible canonical geometry traditionally featuring low turbulence levels. Fractal grids can be used to increase the turbulent Reynolds number, without any negative impact on other parameters, and to remove the classical problem of a relatively low ratio of turbulent to bulk strain. The use of fractal grids to ameliorate such problems is exemplified for fuel lean combustion with combustion regime transitions achieved through the stabilisation of turbulent premixed flames against hot combustion products. An analysis is presented in the context of a multi-fluid formalism that extends the customary bimodal *pdf* approach to include multiple fluid states. The approach is quantified via simultaneous OH-PLIF and PIV, permitting the identification of five separate states (reactant, combustion product, mixing, mildly reacting and flamelet fluids). The sensitivity of the distribution between the fluid states to threshold values is also evaluated. The work suggests that a consistent treatment of the delineating thresholds is necessary when comparing different types of simulations (e.g. DNS) and experiments for reacting fluids with multiple states. The use of fractal grids in a flame driven shock tube provides a further example and is shown to generate turbulent Re numbers of the order 10^5 for flows with Mach numbers approaching unity. The conditions are of relevance to flame stabilisation in hypersonics and are analysed through OH-PLIF and high speed PIV with optimal fractal grids selected on the basis of maximum flame acceleration.

‡ Corresponding author: p.lindstedt@imperial.ac.uk

1. Introduction

The application of fractals to the analysis of fluid flow is well established. Mandelbrot considered the fractal characteristics of iso–scalars in turbulent flows (Mandelbrot 1975) and intermittency in turbulence (Mandelbrot 1974). Vassilicos and Hunt (1991) reviewed the fractal characteristics of flows, while Meneveau and Sreenivasan (1991) attempted to describe the multi-fractal nature of turbulence dissipation. By contrast, the use of fractal geometry grids to generate bespoke multi-scale turbulence is comparatively recent. Hurst and Vassilicos (2007) conducted parametric studies using different types of fractal grids and showed that higher turbulence intensities, as compared to classical grids with higher blockage ratios, can be generated. The work provided a clear indication of the potential of novel methods for promoting enhanced turbulence intensities. Seoud and Vassilicos (2007) showed that fractal square grids produced homogeneous isotropic turbulence that decayed into a single length scale that remained constant with downstream distance. This was further confirmed by Stresing et al. (2010). It was also shown that fractal square grids create a qualitatively different type of turbulence. Direct Numerical Simulations (DNS) were used by Laizet et al. (2009, 2010) to further illustrate the potential of fractal grids to generate elevated levels of turbulence. Subsequent studies have been extended to consider interscale energy transfer in decaying turbulence (Laizet et al. 2013) and the non-equilibrium region (Valente & Vassilicos 2014).

Fractal theories have also been applied to analyse the wrinkling of premixed turbulent flame surfaces. Gouldin (1987) derived a model for the turbulent burning velocity using a fractal concept. Lindstedt and Sakthitharan (1991) used a fractal dimension of 7/3 combined with inner and outer cutoff scales equivalent to the Kolmogorov and integral length scales to show that turbulent burning velocities are dependent on the ratio between the laminar burning and Kolmogorov velocities. Despite the use of fractal based analysis techniques, the potential advantages of using fractal grids to generate turbulence in geometries suitable for systematic investigations of turbulent flames is comparatively recent. Geipel et al. (2010) systematically investigated the use of fractal cross grids an opposed jet geometry. The study was conducted using Particle Image Velocimetry (PIV) and hot wire anemometry (HWA) to generate velocity statistics and energy spectra in order to assess the potential of such grids. It was shown that the use of fractal cross grids led to a more than 100% increase in turbulence levels, with a potential for further increases, leading to a corresponding reduction in ratio of bulk to turbulent strain and thus enabling extended studies of turbulent flames in the opposed jet configuration. Subsequent studies include the structure of turbulence in lean premixed flames (Goh et al. 2013a), the determination of scalar fluxes and conditional statistics (Goh et al. 2014) and turbulent transport in flames approaching extinction (Goh et al. 2015). In addition, studies using rod stabilisation (Soulopoulos et al. 2013) and low-swirl combustion (Verbeek et al. 2015) have appeared suggesting potentially wider application.

The above studies have considered conventional flames. However, combustion technologies operating in the absence of distinct flame fronts are expected to lead to improved control, reduced fuel consumption through stable fuel lean operation, low maximum temperatures and reduced emissions. Such developments induce the need to extend laboratory research to significantly higher turbulence levels and reduced Damköhler (Da) numbers to provide fundamental understanding of combustion regime transitions including distributed and/or flameless regimes, e.g. (Dally et al. 2002, Parente et al. 2011). The opposed jet geometry has been extensively utilised to investigate – laminar as well as turbulent – non-premixed, partial premixed, and premixed combustion and, more recently, combustion regime transitions for aviation fuels (Goh et al. 2013b). The configuration has notable advantages for combustion studies (Mastorakos et al. 1995, Geyer et al. 2005, Geipel et al. 2010): (i) excellent optical access for laser-based diagnostic measurements, (ii) accurate experimental control of boundary conditions, (iii) aerodynamic flame stabilisation, rather than via pilot flames, leading to flame dynamics and extinction being related to the inherent aerothermochemistry of the combustion process; and (iv) individual control of variables affecting the chemical and turbulent time-scale. The last two points identify the facility as ideal for investigations of combustion regime transitions.

Combustion regime transitions are considered here by using data that permits an extension of arguably the most successful statistical description of turbulent premixed combustion, the two-fluid Bray-Moss-Libby (BML) model (Swaminathan & Bray 2011), to a multi-fluid based formulation. The statistical description of combustion approaching distributed reaction zones necessitates a more complex methodology as significant reaction zone broadening and intermediate fluid states are expected. Such effects have recently attracted attention in terms of the impact on scalar gradients (Goh et al. 2013b, Minamoto & Swaminathan 2014). The current work utilises a back–to–burnt opposed jet configuration, with fractal grids for enhanced turbulence generation, to investigate the impact of the chemical timescale on the combustion regime transition for lean premixed flames. A multi–fluid approach (Spalding 1996) is quantified statistically via simultaneous hydroxyl radical planar laser induced fluorescence (OH - PLIF) and PIV/Mie scattering. The approach permits the identification of five fluid states (reactant, combustion product, mixing, mildly reacting and flamelet fluids) and a range of Da numbers, from the conventional propagating flamelet regime well into the distributed reaction zone regime, are investigated. Böhm et al. (2009) and Goh et al. (2013a, 2013b, 2014) have shown that the combination of PIV and OH–PLIF can be used to obtain velocity–scalar statistics describing the dynamics of opposed jet flames approaching extinction and the techniques form the basis for the investigations reported here.

The success of fractal grids in generating stronger turbulent flames though enhanced (multi-scale) wrinkling suggests a potential use in the context of compressible flows. The acceleration of confined flames to strong quasi-stable deflagrations (Lindstedt &

Michels 1989) or detonations is primarily governed by flow conditions (i.e. turbulence intensity), but also depends on mixture reactivity. The influence of obstructions in confined flame tubes, e.g. obstacle shape and blockage ratio (BR), have been the subject of a large number of studies (e.g. Lee et al. (1984), Alekseev et al. (2001), Silvestrini et al. (2008) and Ciccarelli & Dorofeev (2008)). Results show that increasing the BR gives rise to higher flame speeds, due to increased turbulence generation, up to an optimal point where a further increase results in (partial) flame quenching and momentum loss (Beauvais et al. 1994). Due to experimental challenges, the applied diagnostics is typically confined to pressure traces and flame arrival times. However, flow and turbulent velocities obtained in a flame tube featuring baffle-like obstacles have been reported (Lindstedt & Sakthitharan 1998).

The reactivity of a mixture is dependent on fuel properties and initial conditions (e.g. mixture stoichiometry, temperature and pressure) and has been investigated for a number of fuels (Beauvais et al. 1994, Ciccarelli & Dorofeev 2008). Studies concerning fuel mixtures are of increasing interest as fuel blending holds significant potential for further enhancement of combustion processes (Williams et al. 2007, Lieuwen et al. 2008). For example, the addition of H_2 to CH_4 results in a lower effective activation energy and increased flame speed. The current study investigates the use of cross fractal grids (CFGs) to enhance flame acceleration in stoichiometric mixtures of 75% H_2/25% CH_4 with air. The CFGs are installed close to the ignition end to intensify turbulence in the unburned mixture ahead of the advancing flame and is followed by a solid 50% BR obstacle (Lindstedt & Sakthitharan 1998). The optimal CFG characteristics are also investigated.

In summary, the current contribution builds on earlier studies of isothermal and combusting flows in the opposed jet geometry (Geipel et al. 2010, Goh et al. 2013a, Goh et al. 2014, Goh et al. 2015) to cover lean premixed flames burning against hot combustion products (Goh et al. 2013b). Past studies are extended through the use of fractal grid generated turbulence to quantify the transition from a conventional turbulent flame in the flamelet regime of combustion to a distributed mode using a multi-fluid description. The application of fractal grids is further exemplified using a flame driven shock tube where such grids are used to generate peak turbulent Reynolds (Re_t) numbers of the order 10^5 for flows with Mach numbers around unity. The latter set of conditions is of relevance to flame stabilisation in hypersonic devices and is analysed through high speed flame chemiluminescence and high speed PIV with optimal fractal grids selected on the basis of maximum flame acceleration and explosion over–pressures.

2. Experimental Configurations

Two canonical experimental configurations are used in the present study to illustrate the successful application of fractal grids to combustion applications. A flame driven shock tube is used to study transient flame acceleration processes and the resulting over-pressures.

The high flame speeds achieved are of direct relevance to risk assessments associated with explosion hazards. The geometry results in exceptionally high peak turbulence intensities, relevant to flame stabilisation in hypersonic combustion devices, with estimated peak flow and turbulence Reynolds numbers approaching 10^6 and 10^5, respectively. The resulting flames are highly fragmented and the opposed jet configuration is used to investigate the related combustion regime transitions for conditions where the Da number is below unity. The experimental facilities are outlined below.

2.1. Flame Driven Shock Tube

A schematic of the flame driven shock tube with a rectangular cross section (dimensions $0.072 \times 0.034 \times 4.420$ m) is shown in Fig. 1. A number of CFGs, see Table 1, featuring different blockage ratios (BR) and different ratios of the thickest to thinnest bar width (t_r) were evaluated following the findings of Vassilicos and co-workers (Vassilicos & Hunt 1991, Seoud & Vassilicos 2007, Hurst & Vassilicos 2007). An example of a fractal grid is shown in Fig. 2. The grids were mounted at a distance of 115 mm from the ignition end and followed by solid obstacle (BR = 0.50) placed at the bottom of the flame tube at 402.5 mm. The large length to hydraulic diameter (D_h) ratio ($\sim$96) of the tube allows the investigation of flame-obstacle interactions without interference from acoustic waves reflected off the non-ignition end plate for a time window of around 15 ms. The resulting high experimental repeatability is discussed below.

The basic instrumentation included four piezo-electric pressure transducers (3 PCB-113B21 and 1 PCB-113A21; PCB Piezotronics Inc.) and 12 custom made coaxial ionisation probes mounted along the flame tube as specified in Table 2. Both devices feature a recording rate of 1 MHz. The ionisation probes, used extensively in the past (Lindstedt & Michels 1988, Lindstedt & Michels 1989, Lindstedt & Sakthitharan 1998), serve as flame detection devices and provide complementary data on the flame propagation. A 10 kHz high speed particle image velocimetry (HS-PIV) system, featuring a resolution of 576×480 pixels (here corresponding to a 76.0×63.3 mm window) and controlled by LaVision Davis HS 8.0, was used to obtain flow velocities in the shear layer above and in the recirculation zone behind the solid obstacle. The system (Edgewave IS II Nd:YAG laser, Photron Fastcam SA6) was timed and synchronised by an external LaVision HS controller. The camera was equipped with a 105 mm Nikkor camera lens (f5.6) with a mounted 3 nm narrow bandwidth filter for a wavelength of 532 nm. The light sheet, indicated by the green rectangle (W2) in Fig. 1, was directed vertically from the top into the optical section of the flame tube. The silicon oil seeding (droplet size < 1.5 μm) was introduced along with the flow through the inlet pipe. The timing between the double laser pulses was found to be optimum at $\Delta t = 15$ μs. A Photron Fastcam SA3 equipped with a 105 mm Nikkor camera lens (f5.6), without the narrow bandwidth filter, was utilised to investigate the flame passing through the CFG by means of chemiluminescence measurements at a repetition rate of 2.5 kHz. The

interrogation region for the chemiluminescence measurements was set to 99.0×66.5 mm featuring a resolution of 1024×688 pixels. Before each experiment the flame tube was flushed with air and evacuated to a pressure below 0.5 kPa. A partial pressure method was applied to control the required proportions achieving a stoichiometric fuel/air mixture at an initial pressure (P_I) of 45 kPa ($P_I = 1$ atm for the chemiluminescence measurements). Mixture homogeneity was achieved by flow circulation using a diaphragm pump for 28 tube volumes. The mixture was left to settle to achieve quiescent conditions before ignition. All data acquisition devices were triggered using TTL pulses ensuring synchronisation of events. This experimental procedure assured excellent experimental repeatability.

2.2. Opposed Jet Geometry

The opposed jet configuration (Geipel et al. 2010, Goh et al. 2013b) was slightly modified (see Fig. 3) to accommodate seeding of the lower nozzle (LN) by a combination of a flame stabilising mesh (FSM) and a flash back arrestor (FBA). Furthermore, the LN is elongated from 50 to 100 mm. Premixed H_2 ($\Phi = 1.0$) flames, heavily CO_2 diluted for temperature control, are stabilised on the FSM, located 100 mm upstream the LN exit providing hot combustion products (HCP) to the stagnation plane. The aerodynamic stabilisation of the stagnation plane in the proximity of the burner centre is realised by matching the momentum of the LN HCP stream and the upper nozzle (UN) unreacted premixed fuel-air mixture. Consequently, an UN cold gas velocity of $U_{b,UN} = 10.0$ ms^{-1} at 293 K (11.0 ms^{-1} at 320 K) necessitates a $U_{b,LN} \approx 4.3$ ms^{-1} (at 293 K) resulting in an HCP LN exit velocity of ~ 21 ms^{-1}. A cross fractal grid (CFG; see Fig. 4) was installed 50 mm upstream the UN exit, featuring a BR of 65% with maximum and minimum bar widths of 2 mm and 0.5 mm ($t_r = 4$). The CFG provides increased multiscale turbulence (Goh et al. 2013b, Geipel et al. 2010, Goh et al. 2013a, Goh et al. 2014) compared to conventional perforated plates. Premixed CH$_4$–air mixtures with $U_{b,UN} = 11.0$ ms^{-1} at $T_{UN} = 320$ K were injected through the UN at varying equivalence ratio ($\Phi = 0.20, 0.40, 0.60$ and 0.80).

The velocity fluctuations ($u_{rms} = 1.45$ ms^{-1}) and the integral length scale of turbulence ($L_I = 4.1$ mm) were measured using hot wire anemometry, resulting in a turbulent Reynolds number Re$_t \approx 350$ (with kinematic viscosity (ν) of $\sim 1.8 \cdot 10^{-6}$ for air at 320 K). Simultaneous OH – PLIF and PIV measurements were carried out using the technique of Kerl et al. (2011) (two light sheets; 281.7 nm and 532 nm; height = 1D; thickness < 0.5 mm; $\Delta t = 25$ μs). The interrogation regions for the OH – PLIF and PIV cameras were set to 51.9×38.6 mm and 34.5×25.6 mm (1376×1023 pixels). Aluminium oxide (Al$_2$O$_3$) powder ($\rho_a = 3900$ kg/m^3), with particle diameters of $d_{a,50} = 0.44$ μm and $d_{a,90} = 1.66$ μm, was used as velocity tracer particles. For each condition, 3000 double frame image pairs were recorded with the OH – PLIF images obtained from the first laser pulse. Multi-pass cross-correlation PIV with adaptive interrogation regions (IR) and decreasing window size (128×128 to 48×48 pixels) was performed as it offers the

highest accuracy, good spatial resolution and robustness at the penalty of significantly increased calculation time. The smallest IR (48 × 48 pixels and 75 % overlap) was evaluated using the adaptive IR, i.e. change in shape from a round weighted windows to an elliptical Gaussian bell to incorporate the local flow field acceleration. With this method the effective IR size becomes similar to a 24 × 24 window. All passes where calculated using a normalised correlation function with a symmetric shift of both frames. Multi-pass vector post-processing and a universal outlier technique was carried out on the final vector field to eliminate spurious vectors. No vectors were inserted by interpolation to fill-up empty spaces nor was smoothing applied as it could bias the results. The determined vector field consists of 115 x 88 velocity vectors providing a spatial resolution of 0.3026 mm. A multi-fluid post-processing technique (Hampp & Lindstedt 2014) was applied to the simultaneous OH – PLIF and Mie scattering images with the procedure detailed below in Section 2.3. The coordinate system and reference windows, used in the discussion below, are defined in Fig. 5.

2.3. Multi–Fluid Description

Combustion conditions with Da < 1.0 are likely to lead to a broadening of reaction zones and non-flamelet behaviour (Goh et al. 2013b, Minamoto & Swaminathan 2014). Accordingly, two–fluid descriptions assuming thin reaction zones become insufficient. Spalding (1996) formulated a conceptual multi–fluid approach that is here explored using simultaneous PIV and OH – PLIF, which permits the identification of various fluid states associated with the combustion progress. A sample image pair, with PIV vectors overlaid is shown in Fig. 6 and the resulting multi–fluid field is discussed below. A purpose written algorithm detects four iso–contours in each instantaneous image pair in order to distinguish between five different fluid states. The number of images was increased from 1000 (Goh et al. 2014) to 3000 independent realisations in order to improve the statistical accuracy for comparatively rare events.

Reactant Fluid: Fresh reactants emerging from the UN that have not undergone any thermal alternation, i.e. no oxidation or mixing process.

Mixing Fluid: A fluid state that has been exposed to a thermal change, i.e. mixing of the fresh reactants and hot combustion product, without the onset of distinct OH producing chemical reactions.

Mild Reacting Fluid: The high Re_t and low Da investigated, can result in a fluid that is chemically active, but requires thermal support from the hot composition products.

Flamelet Fluid: Regions where conventional propagating flame zones are present.

Product Fluid: Post combustion products resulting from the UN mixture, labeled burnt combustion products (BCP), combined with hot combustion products from the LN.

A conventional density segregation technique (Goh et al. 2013a) allows the identification of unreacted fresh gas (**reactant fluid**, enclosed by the pink line in Fig. 6). Zones where a drop in Mie scattering, yet no OH-signal is detected, indicates an undefined mixing or preheat state without strong chemical reaction (**mixing fluid**, zones between the pink and yellow line). A normalised OH signal, using the signal level within the LN reference window (Fig. 5), permits the identification of HCP and BCP (**product fluid**, enclosed by the yellow line). Conventional propagating flamelets (**flamelet fluid**, enclosed by the red line) are characterised by a strong OH signal and distributed or diffusive reacting fluid by moderate OH levels (**mild reacting fluid**, enclosed by the green line). The distinction between the latter fluid states depends on the signal level and an appropriate threshold definition, corresponding to a thermochemical state, is required as explored below.

2.4. Laminar Flame Calculations and Threshold Definition

Two OH threshold are required corresponding to (i) combustion products ($\Delta_{OH,prod,\Phi}$) and (ii) to conventional propagating flames using a selected themochemical state (e.g. corresponding to the level "close" to the extinction strain rate ($\Delta_{OH,flt,\Phi}$)). The OH signal can then be classified into three intensity zones: (i) product fluid $\leq I_{OH,prod,\Phi}$ (defined in Eq. (1)), (ii) flamelet fluid $> I_{OH,flt,\Phi}$ and (iii) mild reacting fluid $I_{OH,prod,\Phi} < I_{OH,mild,\Phi} < I_{OH,flt,\Phi}$. All intensities ($I_{...}$) correspond to intensity levels obtained from the experimental data while all OH concentrations ($OH_{...}$) are inferred from laminar flame calculations and represent theoretical OH radical concentrations in ppm. The following discussion details the link between $I_{...}$ and $OH_{...}$ for each fluid state.

$$I_{OH,prod,\Phi} \leq \Delta_{OH,prod,\Phi} \cdot I_{OH,ref} \tag{1}$$

Reference State: To estimate fluid type boundaries, a reference state, which exhibits a known and constant OH concentration (OH_{ref}), is defined at a fixed location (dashed rectangle in Fig. 5). The corresponding value was estimated using a laminar flame calculation of a freely propagating flame replicating the experimental conditions of the lower in-nozzle flow (e.g. reactant composition and residence time). The measured nozzle exit temperature of 1700 K (discussed below) was matched using a 10 % heat loss via a radiation correction (Jones & Lindstedt 1988). The resulting $OH_{ref} \approx 800$ ppm was combined with the corresponding experimental OH signal intensity $I_{OH,ref}$ to estimate other fluid state (FS) intensities ($I_{OH,FS,\Phi}$) via Eq. (2).

$$I_{OH,FS,\Phi} = \frac{OH_{FS,\Phi}}{OH_{ref}} \cdot I_{OH,ref} \tag{2}$$

Battles and Hanson (1995) found that the fluorescence signal is nearly proportional to the absorbing OH mole fraction for temperatures in excess of 1600 K. Hence, a ratio defined as unity at 1600 K reduces to 0.9 at 2000 K and is linear in between. It was further shown that the dependency of the OH collision cross section with CO_2, O_2, and H_2O on temperature is significantly reduced for the temperature range of interest (T > 1200 K). Although, the relationship between fluorescence signal and absorbing OH mol fraction depends on the excitation transition, the above linear correlation of Eq. (2) is expected to be reasonable over a comparatively wide range ($1200 \leq T(K) \leq 2200$) for the current Raman technique (Kerl et al. 2011). Further, in the current work the relationship is used to define a fluid boundary based on a relative intensity and not to obtain an absolute concentration.

Product Fluid: The product fluid is here defined as the maximum of the HCP from the LN and the BCP of the UN flames.

HCP Laminar flame calculations were used to estimate the OH concentration of the HCP (OH_{HCP}). The temperature at the LN exit ($\overline{T_{HCP}} = 1700$ K) was measured using thermocouples and the corresponding peak-to-peak temperature fluctuations were 15 K (rms of ~ 3.5 K). The experimental mean temperature was matched by computations using a heat loss factor of 10 % and the modest temperature fluctuations translate to an uncertainty in the OH concentration of $\sim 7\%$.

BCP The HCP were maintained constant throughout this study. However, the OH concentration of the burnt combustion products of the CH_4 flames ($OH_{BCP,\Phi}$) vary with the equivalence ratio. To establish the theoretical $OH_{BCP,\Phi}$ for each case, laminar flame calculations (10 % of the experimental bulk strain) using a counterflow geometry were carried out using the methodology of by Jones and Lindstedt (1988).

The estimated maximum OH concentration ($OH_{prod,\Phi} = \max(OH_{HCP}, OH_{BCP,\Phi})$ in the products was used to define a threshold ($\Delta_{OH,prod,\Phi}$) via Eq. (3) and the corresponding OH signal intensity ($I_{OH,prod,\Phi}$) was assigned to the product fluid.

$$\Delta_{OH,prod,\Phi} = \frac{OH_{prod,\Phi}}{OH_{ref}} \tag{3}$$

Actual threshold values are listed in Table 3 with the impact of uncertainties in the threshold values is discussed below.

Flamelet Fluid: The theoretical OH concentrations of the flamelet fluid ($OH_{flt,\Phi}$), were determined separately for all investigated conditions (e.g. fuel variations and LN conditions) using same laminar counterflow configuration (Jones & Lindstedt 1988). The procedure to determine $OH_{flt,\Phi}$, and subsequently $\Delta_{OH,flt,\Phi}$, is schematically depicted in Fig. 7 and detailed below.

- Lower nozzle (LN) exit conditions are determined from Fig. 7a and assigned as the left hand side boundary condition (BC) in Fig. 7b.

- Right hand side BC match the experimental test case (e.g. in terms of stoichiometry) as shown in Fig. 7b.

- The laminar equivalent of the experimental configuration is replicated to establish a reference OH concentration (OH_{lam}) defined at a specific rate of strain (a_{lam}) as shown in Fig. 7c.

- The computational rate of strain rate is gradually increased for each mixture reactivity and the resulting maximum OH concentration (OH_{peak}) is shown in Fig. 7c.

- The additional OH concentration from the LN (OH_{ref}) is removed by performing calculations for the same strain rate variation for the case $\Phi = 0.00$, with the resulting profile aligned and subtracted from the reactive cases.

- A characteristic strain rate ($a_{crit,\Phi}$) is defined for each mixture (e.g. a $= 450$ s^{-1} for $\Phi = 0.60$) and the corresponding OH concentration ($OH_{flt,\Phi}$) is determined.

- The threshold $\Delta_{OH,flt,\Phi}$ is evaluated based on $OH_{flt,\Phi}$ and the reference concentration (OH_{ref}).

$$\Delta_{OH,flt,\Phi} = \frac{OH_{flt,\Phi}}{OH_{ref}} \leq \frac{I_{OH,flt,\Phi}}{I_{OH,ref}} \tag{4}$$

$$I_{OH,flt,\Phi} \geq \Delta_{OH,flt,\Phi} \cdot I_{OH,ref} \tag{5}$$

The above definition suggests that conventional flamelet–like burning is unlikely at strain rates exceeding $a_{crit,\Phi}$ due to the rapid decay of the OH radical concentration. At lower rates of strain, an increased OH radical concentration is expected, resulting in an uncertainty ($\delta_{OH,flt,\Phi}$) associated with the threshold ($\Delta_{OH,flt,\Phi}$).

Based on the computations reported in Fig. 7, a characteristic change in laminar flame mode is initialised at strain rates > 525 s^{-1} for $\Phi = 0.80$ and > 450 s^{-1} for $\Phi = 0.60$ shown by the maximum OH concentration (Fig. 7c) and laminar burning velocity data (Fig. 7d). At higher rates of strain, the maximum OH concentration and S_L collapse and become insensitive to the mixture reactivity. This implies that the flame is governed by the counter flowing hot combustion products and consequently mark a transition away from a self–propagating flame.

The regime transition is also evident from Fig. 7e, which shows the computed temperature along the domain length at varying rates of strain. The CH_4 mole fraction is superimposed as a colour code. It is evident that, although the fuel is equally consumed, no excess temperature compared to that of the HCP is present. This can be explained by

Fig. 7f, which shows the sum of the CH_4 reaction rates in same frame, but with the H_2O mole fraction colour coded (similar plot for CO_2 colour coding). At low rates of strain, the fuel oxidation reactions occur in an environment with low diluent concentration resulting in a distinct fuel consumption region. At increasing rates of strain the diluent fraction within the reaction zone is significantly increased and the CH_4 consumption rate drops sharply. Accordingly, the combustion process is governed by the hot combustion products. Hence, the process has undergone a clear regime transition. It is worth pointing out that the indicative rate of strain is here based on the axial bulk strain rate. Thus, effects of the radial and local rates of strain are not incorporated. Consequently, actual rates can be expected to be significantly larger.

The maximum OH levels for each respective Φ and characteristic strain rate can be related to the OH reference level (OH_{ref}), see above, with the resulting flamelet threshold (c.f. Eq. (5)) listed in Table 3. No self-propagating flame is expected at lower equivalence ratios, i.e. $\Phi = 0.40$ and 0.20, as these values can be expected to be increasingly beyond the practical (strained) lower flammability limit as supported by the laminar flame data shown in Figs. 7c and 7d. Hence, the introduction of a flamelet threshold ($\Delta_{OH,flt,\Phi=0.2,0.4}$) does not appear meaningful.

Mild Reacting Fluid: Based on the above discussion, the OH concentration and experimental intensities for the mild reacting fluid state can readily be defined:

$$I_{OH,prod,\Phi} < I_{OH,mild,\Phi} < I_{OH,flt,\Phi} \tag{6}$$

The sensitivity of the probability distribution between the different fluid states to the estimated threshold values is discussed below.

2.5. Estimated Damköhler Numbers

The laminar flame data can be combined with the experimental turbulence conditions, i.e. $l_I = 4.1$ mm and $u_{rms} = 1.45$ ms^{-1}, to estimate the Damköhler numbers via Eq. (7).

$$Da = \frac{S_L \cdot l_I}{u_{rms} \cdot \delta_f} \tag{7}$$

The Da number is dependent upon the rate of strain and values at 75 s^{-1} are shown in Table 6. At high rates of strain, the flame parameters (S_L and δ_f) and consequently the Da, become independent of Φ at a constant turbulent timescale. Consequently, the value becomes strongly dependent on the hot combustion products (e.g. T and composition) at high rates of strain (e.g. > 525 s^{-1}) as would be expected in the current back-to-burnt geometry. For the present investigation Damköhler numbers from $0.1 < Da < 1.6$ are realised when based on the lower strain rate of 75 s^{-1}.

2.6. Sensitivity Analysis

The impact of threshold definitions on the current multi–fluid analysis was explored using a sensitivity analysis. The movement of the iso–contour (see Fig. 6) vanishes within the line thickness and is consequently not depicted, but considered in the sensitivity analysis.

The mild reacting fluid threshold ($\Delta_{OH,prod,\Phi}$) is initially varied between 1.6 – 2.4, i.e. from below the uncertainty associated with heat losses (~ 1.7) up to a 50 % increase from the starting value. The sensitivity to the threshold value for the mild reacting fluid probability is shown in Fig. 8a for $\Phi = 0.60$. It evident that with an increasing threshold, the peak probability of the mild reacting fluid is reduced, yet the spatial extent and general trend of the distribution is preserved. In the subsequent work, a value $\Delta_{OH,prod,\Phi\leq0.6} = 2.0$ ($\Delta_{OH,prod,\Phi=0.8} = 3.0$) is preferred as this also ensures that the mild reacting fluid probability is zero for the non-reactive case ($\Phi = 0.0$). Lower values of $\Delta_{OH,prod,\Phi}$ can indicate fictitiously chemically active fluid for the non-reactive case.

The sensitivity of the flamelet distribution was investigated for the case of $\Phi = 0.6$, which is expected to be close to the regime transition and hence potentially the most difficult case to quantify, using a threshold variation between $2.0 < \Delta_{OH,flt,\Phi=0.6} < 3.5$. The lower limit corresponds to utilised product threshold $\Delta_{OH,prod,\Phi\leq0.6}$ and the upper limit to the OH concentration corresponding to a $= 75$ s^{-1}. The results are summarised in Fig. 8b. As expected, the flamelet fluid probability reduces quickly when $\Delta_{OH,flt,\Phi=0.6}$ is increased. However, threshold values below 3.0 are not recommended as the laminar flame calculations suggest a probable transition to a HCP supported combustion process. Accordingly, a limiting value $\Delta_{OH,flt,\Phi=0.6} = 3.0$ is preferred.

The above findings highlight the need to define consistent thresholds for different fluid states when comparing results obtained using different methods. However, despite such considerations it is apparent that for the (most difficult) transitional case of $\Phi = 0.6$, the probability of finding mild reacting fluid in the measurement window is around 20 %, while the probability of finding flamelet fluid is around 15 %. The evolution of all the fluid state probabilities with changes in the stoichiometry (i.e. Da number) is discussed below.

3. Results and Discussion

The use of CFGs to enhance combustion processes and to extend the range of conditions that can be studied is exemplified below. In Section 3.1 the impact on transient flame acceleration and the resulting over–pressure is investigated. The highly fragmented flame fronts detected suggests the need to study combustion regime transition by means of varying the chemical timescale. This is discussed in Section 3.2 by means of a modified opposed jet configuration and a recently introduced multi-fluid approach that has been shown to be advantageous for turbulent reacting flows with Da < 1 (Hampp & Lindstedt 2014).

3.1. Flame Driven Shock Tube

The expansion of combustion products from the laminar flame kernel, initiated by a spark as shown in Fig. 1, drives the unreacted gas mixture ahead of flame front through the fractal grid, resulting in turbulent flame propagation. The passing of the flame through the CFG leads to a substantial increase in flame surface area as shown for a stoichiometric CH_4–air flame ($P_I = 1$ atm) in Figs. 9a–9h and consequently flame acceleration. The flame passing through the CFG was studied using high-speed (2.5 kHz) flame chemiluminescence measurements with its gradient depicted here. As the flame subsequently approaches the solid obstacle, it first decelerates due to confinement followed by strong acceleration resulting from the enhanced turbulence levels in the recirculation zone behind the obstacle. Two consecutive high speed (10 kHz) Mie scattering images, with PIV vectors superimposed, are shown in Fig. 10 illustrating the flame arrival downstream of the solid obstacle (W2 in Fig. 1). The two images show a distributed (or fragmented) flame. A flame propagation speed of $\sim$350 ms^{-1} can be estimated from the flame front displacement distance and the time separation of the two frames.

From a practical point of view, the initial (laminar) flame propagation is typically the limiting factor in terms of the available test time and the CFG is used to substantially reduce the time requirement for this phase. For the same type of mixture, the time to peak pressure was recorded as 37.5 ms in the absence of the fractal grid (Lindstedt & Sakthitharan 1998), compared to 20 ms with the current configuration. This is crucial, as the overall test time is limited by acoustic wave propagation caused by reflections off the closed end of the shock tube and hence impractical tube lengths can readily result. The time to peak pressure obtained using the single CFG is similar to that obtained through the use of a time-dependent jet located at the ignition end of the tube and driven by a pressurised vessel (McCann 1997). Hence, the current configuration achieves a similar result without the associated complications. In the current work, the reactivity of the mixture is further enhanced by the addition of hydrogen as discussed below. The interaction between pressure wave reflection and flame front occurs between ports P8 and P9 ($x_{P8} = 2.31$ m, $x_{P9} = 3.30$ m) as indicated by the dashed line in Fig. 11b. The uncertainty magnitude beyond this disturbance (Zone B) suggest that recorded data are not reliable and consequently excluded from further analysis. Excellent experimental reproducibility is, however, achieved prior to reflected wave interactions (Zone A). This interaction limits the available test time to $\sim$17 ms in present investigation.

A parametric study was carried out to investigate the impact of the CFG characteristics, i.e. the thickest to thinnest bar width ratio (t_r) and the BR, on the initial turbulence generation and flame acceleration with a view to minimise the time to transition to a turbulent flame. The relevant grids listed in Table 1. The intensity of the initial flame acceleration is dependent upon both parameters. The effect of the BR on the overpressure (P_O) is listed in Table 4. The CFG with the lowest BR resulted in a relative overpressure of

$P_O/P_I \approx 3.5$, while the grid with BR of $\sim 63\%$ featured a relative overpressure ($P_O/P_I \approx$ 3.9), an increase of 10% for the tested mixture of 75% H_2 / 25% CH_4 / $Phi = 1.0$. The optimum CFG in terms of maximum resulting P_O, i.e. Grid 4 with BR $\sim 64\%$, was utilised as a basis for a characteristic parameter (t_r) variation. All grids are listed in Table 1.

It was found that an increasing t_r results in enhanced turbulence levels leading to shorter flame arrival times as shown in Fig. 11b. The flame speeds were inferred from the recorded flame arrival time at adjacent probes with the determined maximum listed in Table 5. It is evident that an increasing t_r results in a higher flame speed with a variation from 304 ± 9 ms^{-1} to 335 ± 30 ms^{-1}, consistent with the resulting overpressure. The CFG featuring the highest t_r leads to a maximum overpressure of 174 ± 4 kPa ($P_O/P_I = 3.9$), while the CFG with lowest t_r results in 147 ± 3 kPa ($P_O/P_I = 3.3$), a decrease of ~ 20 %. Maximum over-pressures for all grids (varying t_r) are shown in Fig. 11a and Table 5.

Grid 6 features a BR similar to the solid obstacle (BR $\approx 52\%$ vs. 50%) and was selected for subsequent experiments. Typical pressure traces can be seen in Fig. 12a. The detected variability of the peak pressure and timing was derived via the root mean square (RMS) from 11 runs. The moderate initial pressure built up, shown in Fig. 12a, results from the flame passing through the CFG. The interim deceleration following the flame exit from the CFG, as discussed above, is also evident in the pressure traces and results in an interim drop in over-pressure as shown in Fig. 12a for pressure transducers P1, P2 and P3 at around 7.0 ms. The flame front approach to the obstacle is followed by rapid acceleration resulting in an abrupt rise in pressure. The average over-pressure at P4, situated just after recalculation zone, is 164 ± 4 kPa with an average pressure wave arrival times of $t_{P4} = 8.9 \pm 0.2$ ms. Considering the transient nature of the process being studied, the magnitude of the recorded uncertainties reflects the excellent reproducibility of the experiments and confirms the suitability of the experimental procedure and that the CFG can be used to increase the range of mixtures studied without any detriment.

Given an initial pressure of $P_I = 45$ kPa the maximum relative over-pressure is $P_4/P_I = 3.7$. The corresponding flame speeds, determined based on the distance between two adjacent probes and their respective recorded difference in flame arrival time, are depicted in Fig. 12b. The uncertainties were determined based on flame arrival times. Due to the locations of P1 and P2, the recorded flame speed at $x_{1.2} = 0.585$ m represents an average value across the solid obstacle and is not the maximum occurring in this region. This indicates that using conventional flame detection devices it is difficult to resolve the local flame speed variations; hence the use of more advanced measuring techniques, e.g. HS-PIV, are essential in the recirculation zone. The highest flame speed is obtained between port P2 and P3 ($x_{2,3} = 1.02$ m) in the order of 350 m/s. The flame arrival time at these ionisation probes coincides to the pressure wave arrival time at the fourth pressure transducer at which the maximum over-pressure is recorded. Hence, the highest over-pressure is recorded at the point where the flame speed reaches its maximum.

HS-PIV at 10 kHz was used to determine the flow acceleration and velocities in the reactants. The technique also enables a qualitative interpretation of the flame surface structure as well as providing planar information on the flame arrival in the interrogation window. The use of silicone oil seeding (Dow Corning Xiameter PMX 200/50cS) leads to flame surface visualisation due to the evaporation of the droplets. The resulting iso-contour is located around 600 K and reasonably close to the $\sim$640 K iso-contour identified by Schlieren imaging (Weinberg 1956). The mean flame arrival time, based on the first occurrence in the optical section, was found to be $t_{fa} = 7.3 \pm 0.1$ ms. This again shows excellent experimental reproducibility and is consistent with the flame arrival times obtained from the ionisation probe data. The extremely fragmented flame surface (see Fig. 10) is apparent from the Mie scattering images. The flame enters the interrogation region in the upper part of the tube, dividing the mixture into burnt (top) and unburnt (bottom) regions, and subsequently circulates back at the bottom into the interrogation region against the main flow direction. The high reproducibility suggests that it is worthwhile to evaluate flow velocities for illustrative purposes. Also shown in Fig. 10a are examples of analysis windows (A, B, and C) used to compute the time evolution of the mean velocity magnitude and velocity components based on Eq. (8), where I and J are dimensions of the analysis windows in x and y direction respectively. The locations of the analysis windows A, B, and C were chosen to represent the velocities in the free flow, shear layer and recirculation zone respectively. Vectors with nil value have been excluded.

$$\overline{u} = \frac{\sum_r^R \sum_i^I \sum_j^J u_{r,i,j}}{R \times I \times J} \quad ; \quad \overline{v} = \frac{\sum_r^R \sum_i^I \sum_j^J v_{r,i,j}}{R \times I \times J}$$

$$|\overline{u}| = \frac{\sum_r^R \sum_i^I \sum_j^J \sqrt{(u_{r,i,j}^2 + v_{r,i,j}^2)}}{R \times I \times J} \tag{8}$$

$$|\overline{u}|_{rms} = \frac{\sqrt{\sum_r^R ((\sqrt{(u_r^2 + v_r^2)} - |\overline{u}|)^2)}}{R}$$

The determined mean horizontal ($\overline{u}$) and vertical ($\overline{v}$) velocity components, as well as the velocity magnitude $|\overline{u}|$ and its RMS value $|\overline{u}|_{rms}$, were obtained from the 11 runs (R) where HS-PIV was carried out and are depicted in Fig. 13b. The approach serves as an illustration of data processing. However, the best way to compare data with time-dependent calculation methods, such as Large Eddy Simulations (LES), is subject to debate. The velocities reported here correspond to the mean flow of reactants just after the flame passes the obstacle. The relatively large uncertainties obtained between $6 - 7$ ms result partly from the slight differences in flame arrival times at the obstacle.

The $|\overline{u}|$ of position A, representing the velocity magnitude of the free flow, exhibits a maximum velocity ($|\overline{u}| = 286 \pm 4$ ms^{-1}) significantly higher than in the shear layer ($|\overline{u}| = 170 \pm 9$ ms^{-1}) (position B). The mean $\overline{u}$ and $\overline{v}$ velocity components within the recirculation zone (window C) are also shown. The initial rise in the horizontal and the moderate increase in the negative vertical velocity components reflect the overall flow

acceleration. The development of the recirculation zone is indicated by the sharp rise in negative $\bar{v}$ after $\sim$6 ms. The rise and eventual inversion to positive values in $\bar{v}$ is a result of the eddy moving downstream - away from the obstacle - with increasing flow velocity. In Fig. 13a, the analysis window C has been shifted downstream while maintaining its size and vertical location, as indicated by the dashed arrow. It is evident that the positive and negative extrema of the vertical velocity component occurs later as the frame is shifted away from the obstacle. However, the magnitude of the vertical negative peak velocities is approximately constant and the strength of the eddy is maintained. The mean local maximum velocity is $\bar{u}_{max} = 432$ ms^{-1} with the absolute maximum $u_{max} = 453$ ms^{-1}. The maximum velocities coincide approximately with the flame arrival in the optical section ($\mathrm{t}_{fa} \simeq 7.3$ ms) and are subject to large stochastic variations due to the intensity of the turbulent explosion. Accordingly, the time axis in Fig. 13b is truncated before this event. Using $\bar{u}_{max}$ and the hydraulic diameter of the tube, a Reynolds number around $5.6 \cdot 10^5$ at $\mathrm{P}_I = 45$ kPa is obtained. Lindstedt and Sakthitharan (1998) determined turbulence intensities of $10 - 20\%$ in an identical device without the CFG allowing an estimate of the turbulent Reynolds number as $Re_t \approx 1.0 \cdot 10^5$. The current results, i.e. an extremely fragmented flame front and high Re_t, are very promising in terms of short flow timescales and consequently reduced Da numbers. However, to actually investigate the related combustion regime transitions in detail, the opposed jet geometry offers significant advantages over the flame driven shock tube as explored below.

3.2. Combustion Regime Transitions

Preceding studies (Goh et al. 2013*b*, Geipel et al. 2010, Goh et al. 2013*a*, Goh et al. 2014) featuring the use of fractal grids has highlighted significant advantages over conventional perforated plates within the opposed jet configuration. Consequently, a CFG is utilised to investigate the combustion regime transition in a highly turbulent environment by means of chemical timescale variations. Applying the methodology detailed in Section 2.3, multiple fluid states can be detected. Such a resulting multi–fluid field, corresponding to the image pair example of Fig. 6, is depicted in Fig. 14 where each colour represents a specific fluid state with the detected iso–contours also drawn:

- Light blue – **reactant fluid**, enclosed by the pink line.

- Dark blue – **mixing fluid**, bordered by the pink and white iso-contour.

- Orange – **mild reacting fluid**, enclosed by the black line.

- Red – **flamelet fluid**, bounded by the red line.

- Green – **product fluid**, restricted by the white iso-contour.

In order to remove minor inconsistencies associated with the experimental alignment, i.e. location of the stagnation plane due to jet momentum matching, the spatial multi–fluid probability is evaluated using the coordinate system (CS) x_s shown in Fig. 5. The origin of the CS is aligned with the density segregation iso–contour (i.e. the first thermal alteration). Consequently, when plotting the **reactant fluid** aligned on $x_s = 0$, the profile sharply drops from unity to zero. As illustrated in Fig. 15a, reactant fluid is also present at $x_s > 0$, with a probability peaking at $\sim L_I/4$ and extending to $\sim L_I$. The qualitative behaviour can be expected due to large eddies penetrating into the reactants and tearing out fluid pockets. The effect appears broadly independent of the mixture reactivity.

The spatial probability of the **mixing fluid** aligned along $x_s = 0$ is depicted in Fig 15b. A sharp rise at the origin is observed, providing evidence of the importance of this fluid state adjacent to the reactant fluid. The mixing fluid probability is reduced away from the origin in favour of chemical reactions, i.e. smaller quantities of HCP are required to initialise chemical activity.

The mild reacting fluid probability, i.e. chemically active fluid yielding a OH-signal concentration below the threshold $\Delta_{OH,flt,\Phi}$, is depicted in Fig. 15c. It is evident that with increasing Φ, its probability is distinctly favoured as shown by the peak and spatial extent. The modest increase between $\Phi = 0.40$ to 0.60 results from the enhancement of flamelet–like propagation and is consequently reflected in Fig. 15d. It is obvious that with increasing reactivity the flamelet fluid is favoured as conventional flame propagation is increasingly realised. The first occurrence of flamelet–like burning is observed at $\Phi = 0.60$. Yet, due to the high turbulence levels in the current aerodynamically stabilised configuration, conventional flame propagation has a modest probability.

4. Conclusions

The current contribution illustrates how the use of (near) optimal cross fractal grids can be used to move experimental conditions closer to those of practical devices while maintaining the optical access advantages associated with laboratory scale experiments. Related studies (Goh et al. 2013b, Geipel et al. 2010, Goh et al. 2013a, Goh et al. 2014) have reported on the advantages of CFGs in combustion applications and the current work expands such work to include high speed turbulent combustion with Re numbers up to 560,000 for stoichiometric hydrogen/methane-air flames. Data obtained using flame detection probes and pressure transducers was supported by 10 kHz HS-PIV and 2.5 kHz high speed chemiluminescence measurements. The combination of measurement techniques provides a comparatively comprehensive analysis of the transient flame acceleration process. Time resolved data of flame arrival times and pressure allowed the discrete identification of the flame acceleration phases initiated by a CFG and a subsequent solid obstacle.

High speed chemiluminescence recordings of flames passing through the CFG reveals

the initial flame fragmentation, which governs the emerging flame propagation speed and overpressure. It was shown that the turbulence intensity and, consequently, the turbulent flame propagation speed are dependent on the CFG characteristics. The CFG with $t_r = 6.7$ results in an increase of the initial pressure rise to 43.1 kPa, compared to 35.3 kPa for $t_r = 1.0$, an increase of $\sim 20\%$. The change is the initial pressure rise is directly correlated to the maximum subsequent over-pressures of 174 ± 4 and 147 ± 3 kPa, respectively. The use of an optimum CFG combined yields a maximum local flame speed of $u_f > 330 \ \mathrm{ms}^{-1}$ showing a highly fragmented flame front verified by means of Mie scattering images. The data further suggest that optimised CFGs allow a significant reduction in the time to the peak pressure, as compared to a configuration without a CFG (Lindstedt & Sakthitharan 1998), while maintaining excellent reproducibility. It is also evident that the resulting flames are highly fragmented. The unreacted gas flow velocities were obtained by means of HS-PIV in the recirculation zone behind the obstacle showing the displacement of the fresh gas by the hot combustion products and the temporal evolution of the recirculation zone.

To study combustion regime transitions, a CFG was utilised for turbulence generation within the opposed jet geometry that features aerodynamic flame stabilisation. A recently introduced multi-fluid description (Hampp & Lindstedt 2014) was used to study combustion regime transitions. The impact of threshold definitions was analysed using detailed laminar flame calculations to link relative OH radical thresholds to the post-processing of experimental data. The findings were supported by a sensitivity analysis with multi–fluid statics determined using a variation in the equivalence ratio. The results show that with increasing reactivity, the probability of mixing is reduced in favour of a mildly reacting fluid and, finally, conventional flame propagation. The work suggests that a consistent treatment of applied threshold levels is necessary when comparing different types of simulations (e.g. DNS) and experiments for reacting fluids with multiple states. However, the work also suggests that such characterisations are possible and useful in delineating combustion regime transitions.

Overall, the results presented here further illustrate the benefits associated with the use of fractal grid generated turbulence in reacting flow environments.

Acknowledgments

References

Alekseev V I, Kuznetsov M S, Yankin Y G & Dorofeev S B 2001 *J. Loss Prev. Proc. Industr.* **14**(6), 591–596.

Battles B E & Hanson R K 1995 *J. Quant. Spectrosc. Radiat. Transfer* **54**(3), 521–537.

Beauvais R, Mayinger F & Strube G 1994 *Int. J. Hydrogen Energy* **19**(8), 701–708.

Böhm B, Heeger C, Boxx I, Meier W & Dreizler A 2009 *Proc. Combust. Inst.* **32**(2), 1647–1654.

Ciccarelli G & Dorofeev S 2008 *Prog. Energy Combust. Sci.* **34**(4), 499–550.

Dally B B, Karpetis A N & Barlow R S 2002 *Proc. Combust. Inst.* **29**, 1147–1154.

Geipel P, Goh K H H & Lindstedt R P 2010 *Flow Turbul. Combust.* **85**, 397–419.

Geyer D, Kempf A, Dreizler A & Janicka J 2005 *Combust. Flame* **143**(4), 524–548.

Goh K H H, Geipel P, Hampp F & Lindstedt R P 2013*a Fluid Dyn. Res.* **45**(061403).

Goh K H H, Geipel P, Hampp F & Lindstedt R P 2013*b Proc. Combust. Inst.* **34**(2), 3311–3318.

Goh K H H, Geipel P & Lindstedt R P 2014 *Combust. Flame* **161**(9), 2419–2434.

Goh K H H, Geipel P & Lindstedt R P 2015 *Proc. Combust. Inst.* **35**(1), 1469–1476.

Gouldin F 1987 *Combust. Flame* **68**(3), 249–266.

Hampp F & Lindstedt R P 2014 *Proc. TNF12* .
    URL: *http://www.sandia.gov/TNF/12thWorkshop/index.php*

Hurst D & Vassilicos J C 2007 *Phys. Fluids* **19**, 035103.

Jones W P & Lindstedt R P 1988 *Combust. Sci. Techn.* **61**, 31–49.

Kerl J, Sponfeldner T & Beyrau F 2011 *Combust. Flame* **158**(10), 1905–1907.

Laizet S, Lamballais E & Vassilicos J C 2010 *Comput. Fluids* **39**(3), 471–484.

Laizet S & Vassilicos J 2009 *Journal of Multiscale Modelling* **1**(1), 177–196.

Laizet S, Vassilicos J & Cambon C 2013 *Fluid. Dyn. Res.* **45**, 061408.

Lee J H S, Knystautas R & Freiman A 1984 *Combust. Flame* **56**(2), 227–239.

Lieuwen T, McDonell V, Petersen E & D. S 2008 *J. Eng. Gas Turbines Power* **130**(1), (011506).

Lindstedt R P & Michels H J 1988 *Combust. Flame* **72**(1), 63–72.

Lindstedt R P & Michels H J 1989 *Combust. Flame* **76**(2), 169–181.

Lindstedt R P & Sakthitharan V 1991 *in* '8th Symposium on Turbulent Shear Flows'.

Lindstedt R P & Sakthitharan V 1998 *Combust. Flame* **114**(3–4), 469–483.

Mandelbrot B B 1974 *J. Fluid Mech.* **62**(2), 331–358.

Mandelbrot B B 1975 *J. Fluid Mech.* **72**(03), 401–416.

Mastorakos E, Taylor A & Whitelaw J H 1995 *Combust. Flame* **102**(1-2), 101–114.

McCann H A 1997 Time-Resolved Measurements of Freely Propagating Turbulent Flames PhD-thesis Imperial College, London.

Meneveau C & Sreenivasan K 1991 *J. Fluid Mech.* **224**(1), 429–484.

Minamoto Y & Swaminathan N 2014 *Combust. Flame* **161**, 1063–1075.

Parente A, Sutherland J C, Dally B B, Tognotti L & Smith P J 2011 *Proc. Combust. Inst* **33**, 3333–3341.

Seoud R E & Vassilicos J C 2007 *Phys. Fluids* **19**(10), 105108–105108.

Silvestrini M, Genova B, Parisi G & Trujillo F J L 2008 *J. Loss Prev. in the Process Industries* **21**(5), 555–562.

Soulopoulos N, Kerl J, Spoonfeldner T, Beyrau F, Hardalupas Y, A M K P T & Vassilicos J C

2013 *Fluid Dyn. Res.* **45**(061404).

Spalding D B 1996 *Comp. Tech. App.* **CTAC95**, 59–81.

Stresing R, Peinke J, Seoud R & Vassilicos J 2010 *Phys, Rev. Lett.* **104**(19), 194501.

Swaminathan N & Bray K N C 2011 *Turbulent Premixed Flames* Cambridge University Press.

Valente P & Vassilicos J 2014 *J. Fluid. Mech.* **744**, 5–37.

Vassilicos J C & Hunt J C R 1991 *P. Roy. Soc. A-Math Phy.* **435**(1895), 505–534.

Verbeek A A, Bought T W M, Stifles G G M, Geurts B J & van der Meer T H 2015 *Combust. Flame* **162**(1), 129–143.

Weinberg F J 1956 *Proc. R. Soc. Lond. A* **235**, 510–517.

Williams T C, Shaddix C R & W. S R 2007 *Combust. Sci. Technol.* **180**(1), 64–88.

Table 1: Investigated CFG geometries where BR is the blockage ratio, t_{max} and t_{min} the maximum and minimum bar width, $t_r = t_{max}/t_{min}$. The diagonal of the cut-out is $d_h = 3.73$ mm and the fractal dimension D = 2.0 mm for all grids.

Grid No.	BR [%]	t_{max} [mm]	t_{min} [mm]	t_r [mm]
1	63.70	1.7	1.7	1.0
2	63.53	3.0	1.25	2.4
3	63.97	4.0	1.0	4.0
4	63.53	5.0	0.75	6.67
5	73.23	4.0	1.50	2.67
4	63.53	5.0	0.75	6.67
6	52.27	4.0	0.50	8.0
7	43.64	2.5	0.50	5.0

Table 2: Port location (X) for installed pressure transducers (P) and ionisation (I) probes or both (PI).

Port	P0	P1	P2	P3	P4	P5	P6	P7	P8	P9	P10	P11	P12
X [m]	0.07	0.27	0.90	1.14	1.37	1.61	1.84	2.08	2.31	3.30	3.60	3.90	4.20
Type	P	PI	PI	I	PI	I	I	I	PI	PI	I	I	I

Table 3: Threshold values as function of Φ.

Threshold	$\Phi = 0.2$	$\Phi = 0.4$	$\Phi = 0.6$	$\Phi = 0.8$
$\Delta OH, prod, \Phi$	2.0	2.0	2.0	3.0
$\Delta OH, flt, \Phi$	N.A.	N.A.	3.0	6.0

Table 4: The impact of the CFG BR on the maximum overpressure (P_o).

Grid No.	BR [%]	t_r [mm]	P_o [kPa]
5	73.23	4.0	166 ± 3
4	63.53	6.67	174 ± 4
6	52.27	4.0	164 ± 4
7	43.64	2.5	158 ± 2

Table 5: The impact of the t_r of the CFG on the maximum overpressure (P_o) and maximum flame speed (u_f).

Grid No.	t_r [mm]	P_o [kPa]	u_f [ms^{-1}]
1	1.0	147 ± 3	304 ± 9
2	2.4	149 ± 2	307 ± 16
3	4.0	160 ± 3	319 ± 29
4	6.67	174 ± 4	335 ± 30

Table 6: Damköhler numbers for varying Φ at characteristic strain rates.

Strain rate	a = 75 s^{-1}			
Φ	0.2	0.4	0.6	0.8
S_L ms^{-1}	0.04	0.05	0.12	0.29
δ_f mm	1.86	1.64	0.95	0.51
u$_{rms}$ ms^{-1}	1.45	1.45	1.45	1.45
L$_I$ mm	4.1	4.1	4.1	4.1
Da	**0.06**	**0.09**	**0.4**	**1.6**
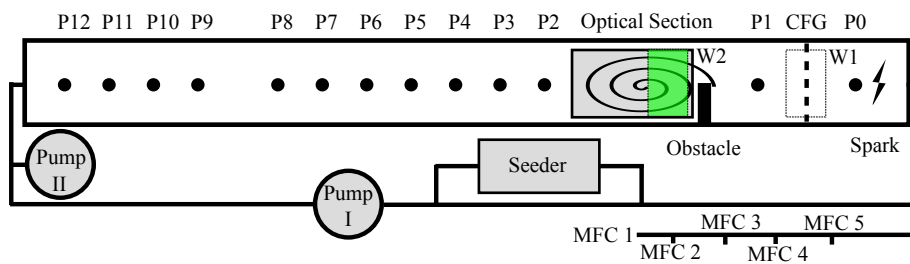
Figure 1: Schematic of the experimental setup with HS-PIV field of view indicated by the green rectangular; MFC - Mass Flow Controller.
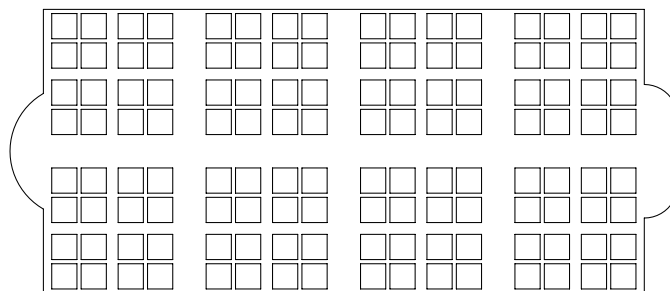
Figure 2: Cross fractal grid (CFG 6) installed as illustrated in Fig. 1.
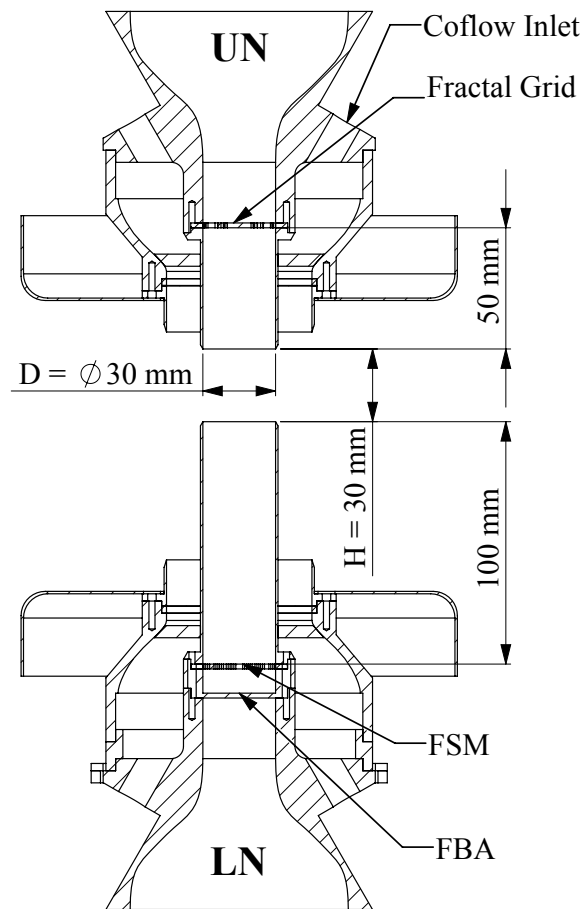
Figure 3: Experimental configuration.
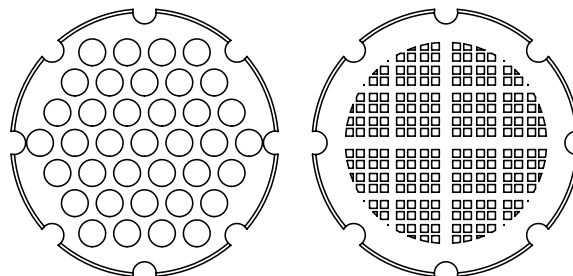
Figure 4: Conventional perforated plate and cross fractal grid.
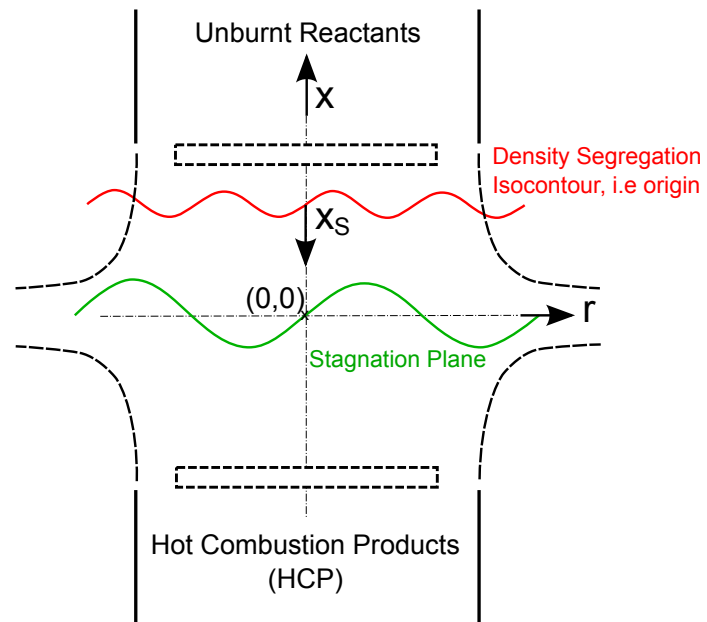
Figure 5: Coordinate system convention and location of reference windows (dashed rectangular areas).
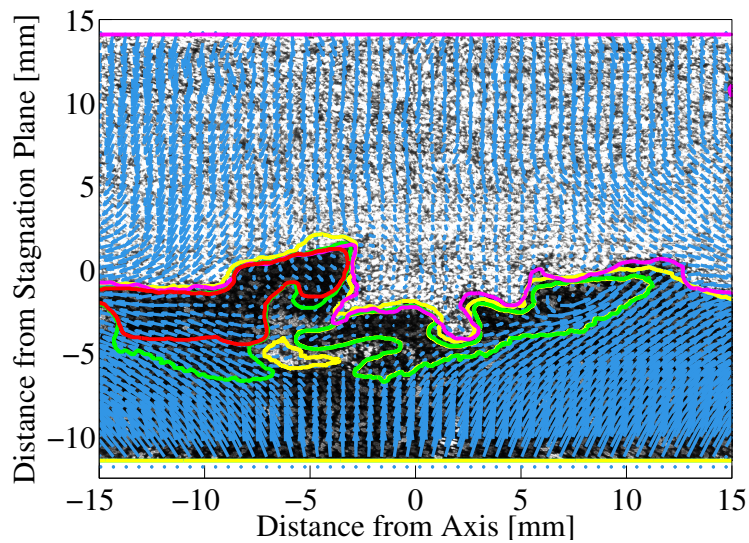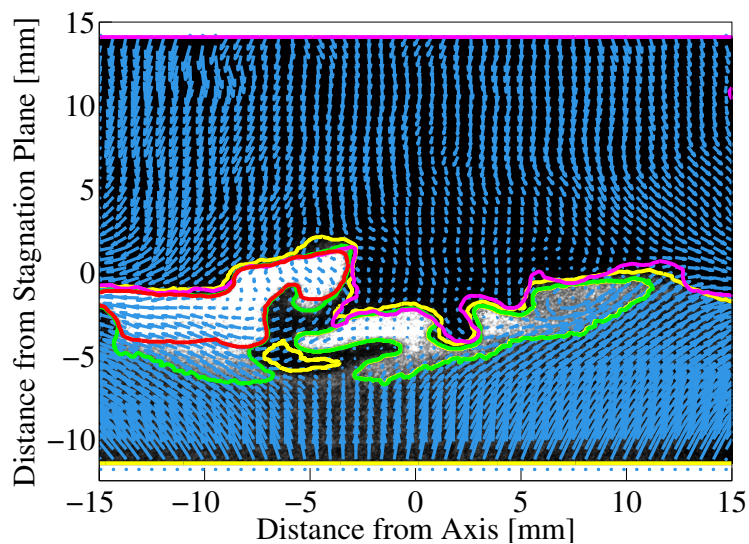
Figure 6: Identification of multi–fluids: (a) Mie; (b) OH signal. The fluid states are **reactant fluid**, enclosed by the pink line, **mixing fluid**, zones between the pink and yellow line, **product fluid**, enclosed by the yellow line, **flamelet fluid**, enclosed by the red line and **mild reacting fluid**, enclosed by the green line.
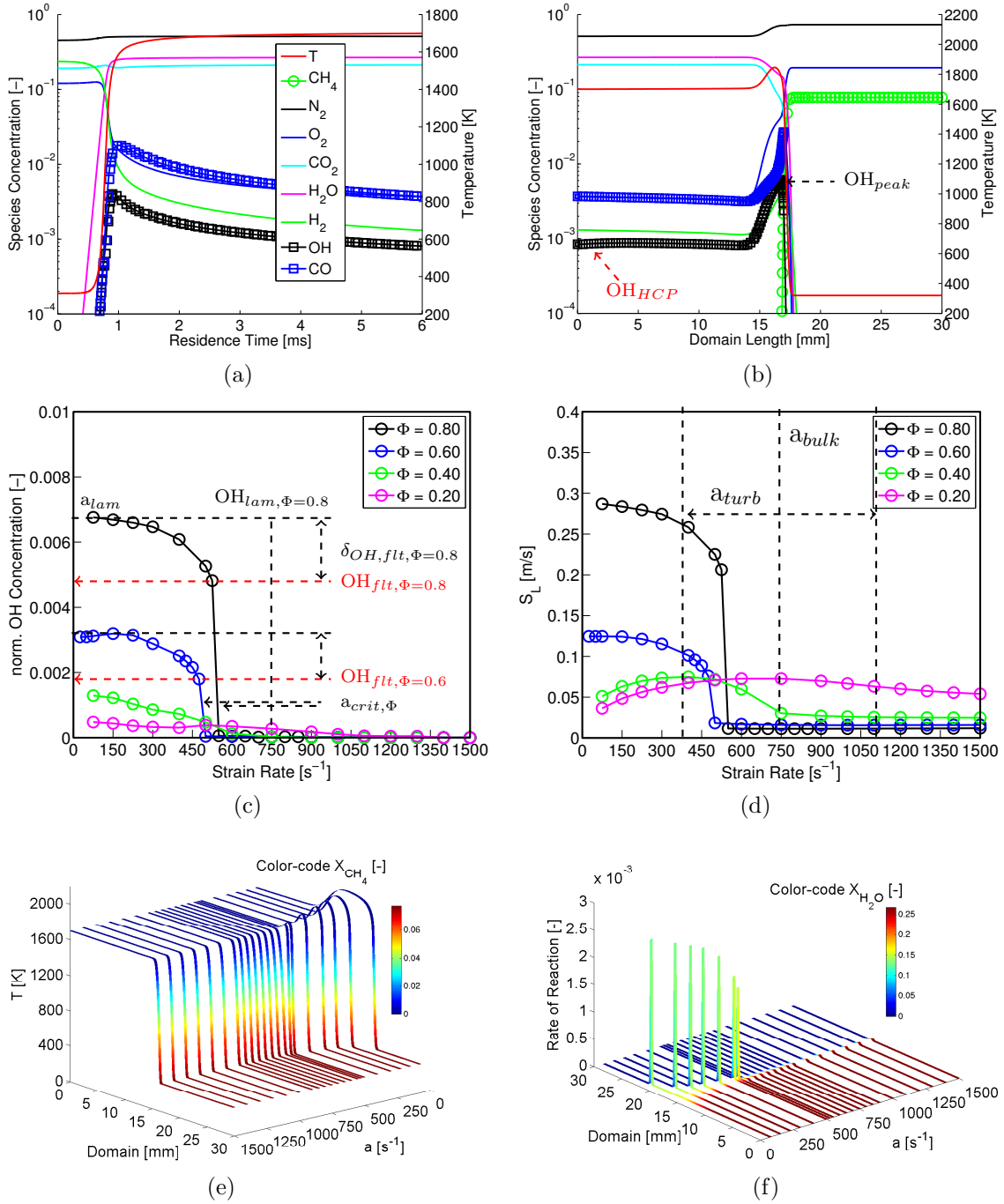
Figure 7: Laminar flame calculation framework to define the threshold OH_{flt}: (a) Freely propagating flame representing the LN; (b) Laminar opposed jet flame at $a = 400$ [s^{-1}] and $\Phi = 0.80$; (c) Maximum OH concentration of a laminar flame rate at varying strain rate; (d) Laminar flame speed S_L at varying strain rate and equivalence ratio; (e) Temperature as a function of strain rate over domain length with CH_4 mole fraction as colour code; (f) Sum of CH_4 consumption reaction rates as a function of strain rate with H_2O mole fraction as colour code.
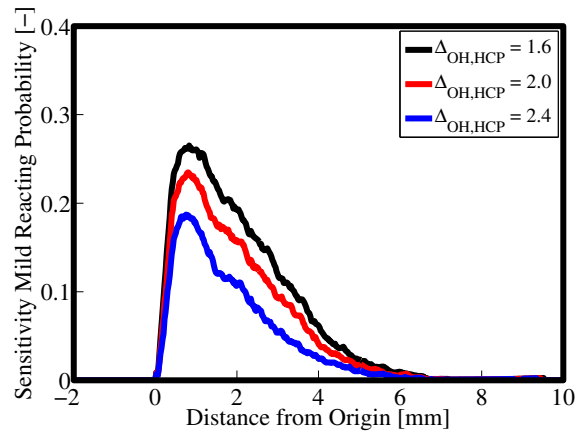
(a)
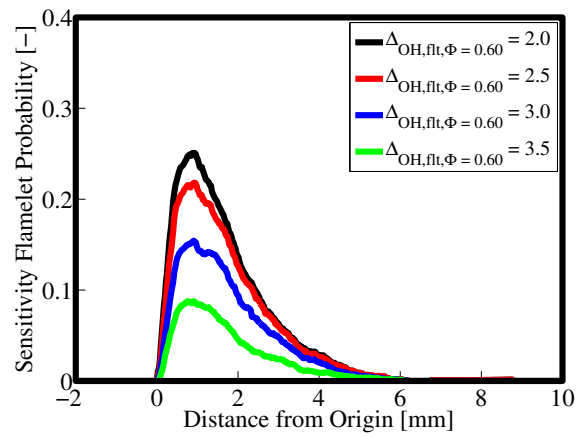
(b)

Figure 8: Sensitivity analysis on thresholds for the case $\Phi = 0.60$: (a) $\Delta_{OH,HCP}$; (b) $\Delta_{OH,flt,\Phi}$.
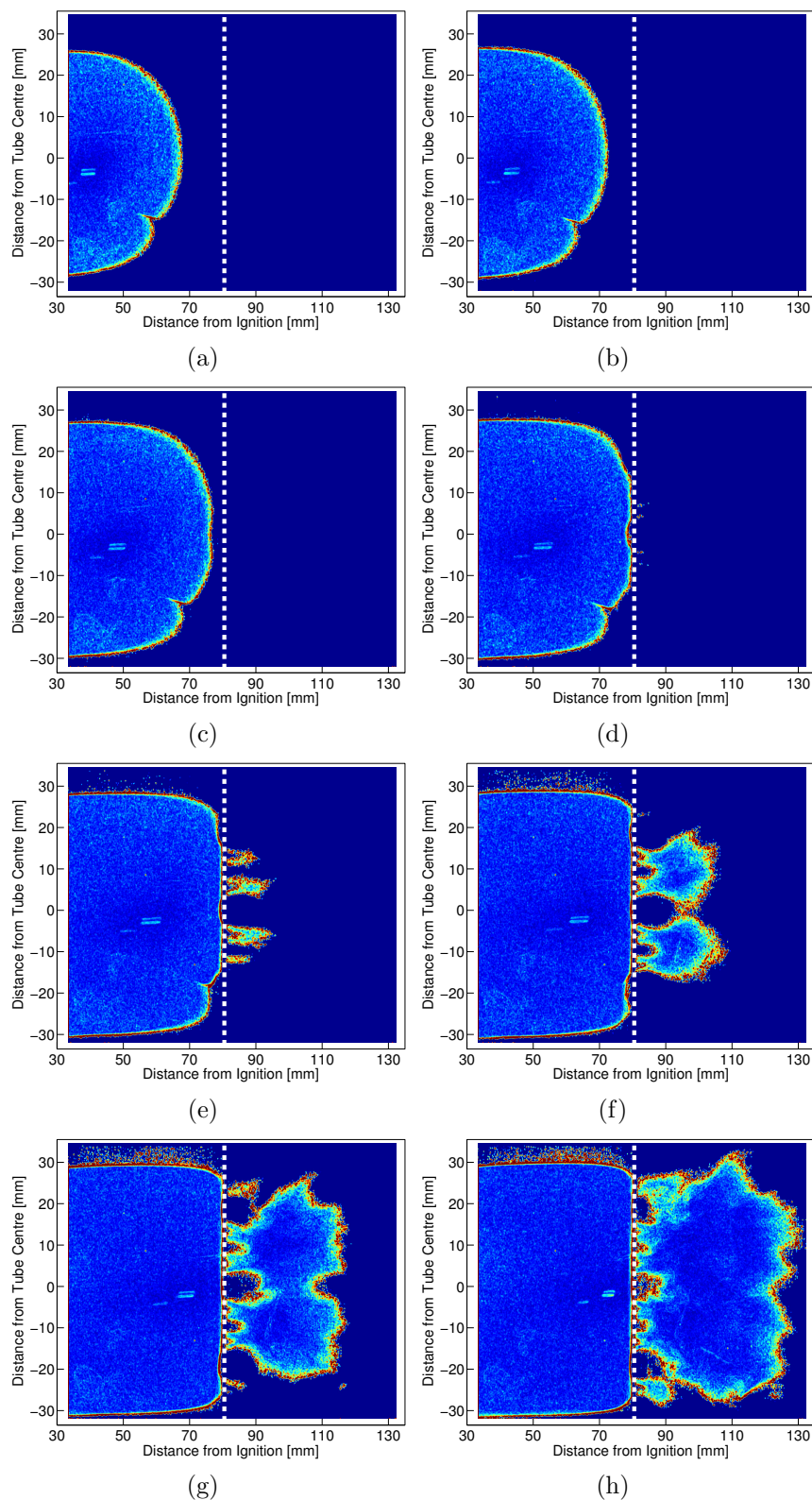
Figure 9: Section of a high speed chemiluminescence measurement time series at 2.5 kHz (gradient analysis) to visualise the flame passing through a CFG of a stoichiometric CH_4-air flame at 1 atm at times: (a) 11.2 ms; (b) 11.6 ms; (c) 12.0 ms; (d) 12.4 ms; (e) 12.8 ms; (f) 13.2 ms; (g) 13.6 ms; (h) 14.0 ms; after ignition, corresponding to window W1 in Fig. 1.

(a)   (b)
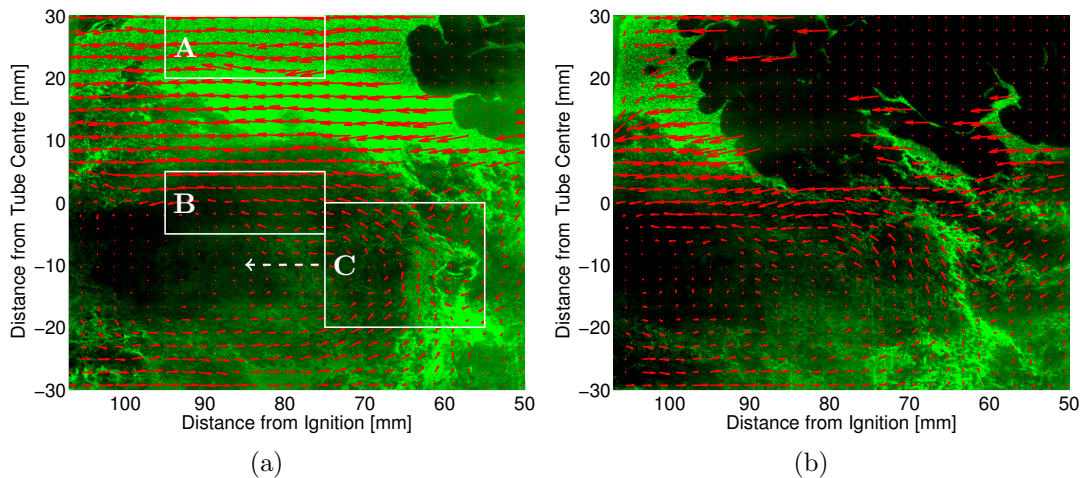
Figure 10: Consecutive high speed Mie scattering images at 10 kHz at: (a) 7.4 ms and (b) 7.5 ms after ignition for a stoichiometric 75% H_2/25% CH_4/air mixture with P_0 = 0.45 bar.

(a)   (b)
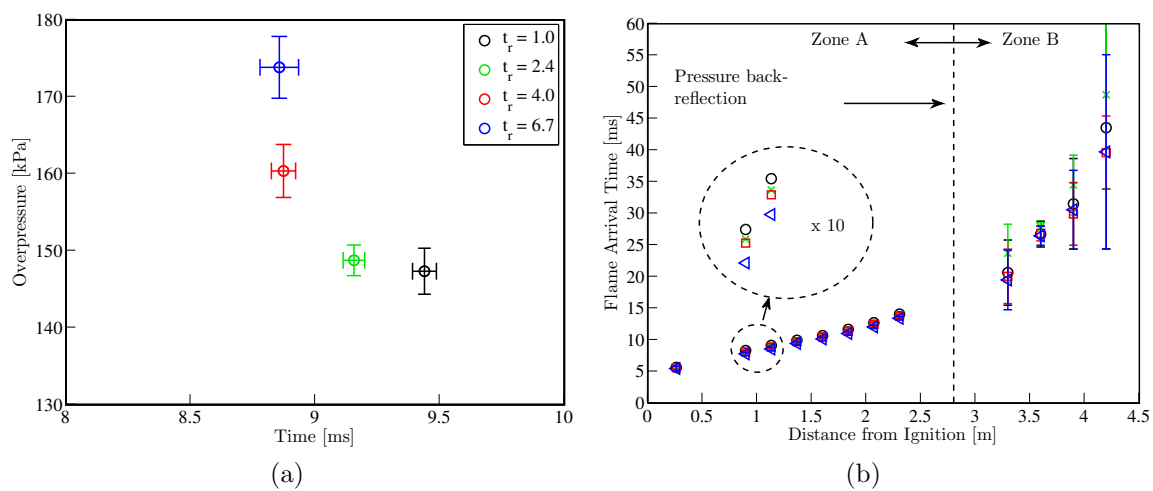
Figure 11: The impact of the CFG t_r on: (a) The maximum overpressure at pressure transducer 4; (b) The flame arrival time. ◁ $-$ t_r = 6.67, □ $-$ t_r = 4.0, × $-$ t_r = 2.4, ○ $-$ t_r = 1.0.

(a)   (b)
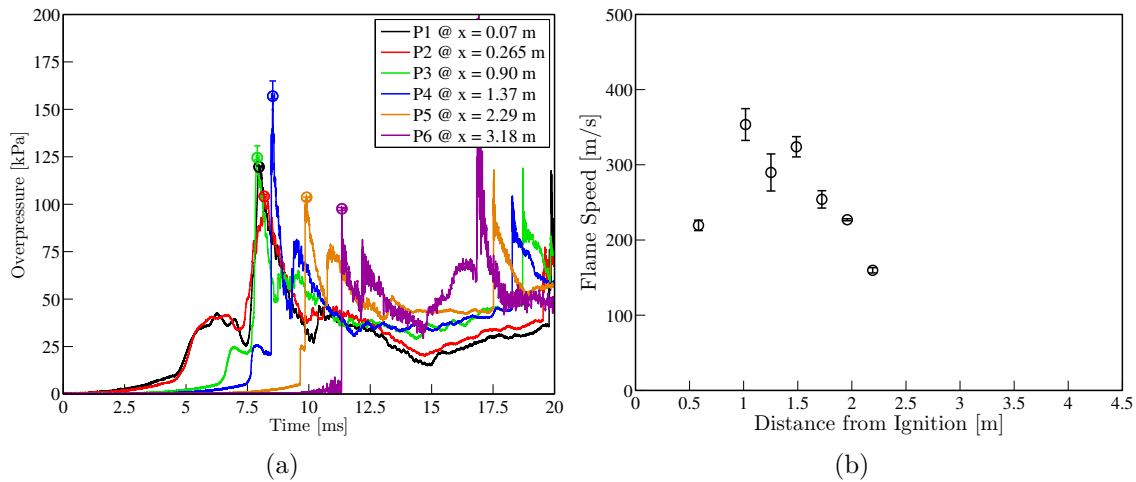
Figure 12: Pressure wave and flame speed measured along the flame tube for CFG 6 with BR $\sim$ 50 % and t$_r$ = 8.0. (a) Over-pressure traces for six transducer obtained from 11 experiments; (b) Average flame speed measured between two adjacent ionisation probes.

(a)   (b)
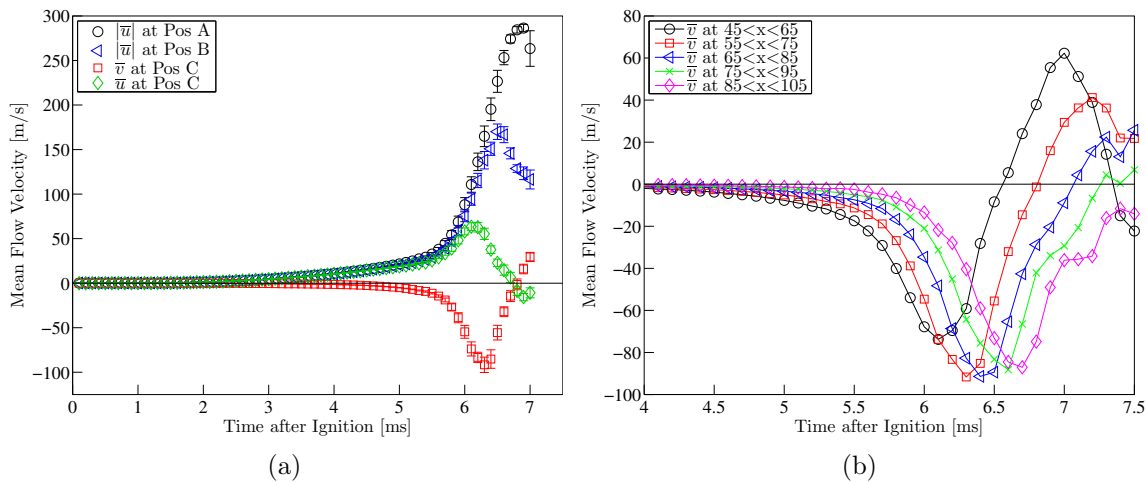
Figure 13: Flow velocity in the reactants: (a) Mean and peak velocities in the selected analysis windows (A,B,C) shown in Fig. 10a; (b) The mean vertical velocity component $\overline{v}$ obtained with window C shifted in the axial direction.
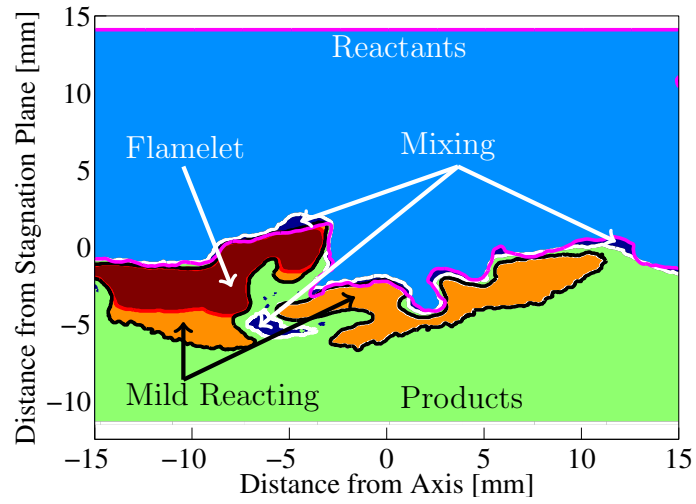
Figure 14: Example of multi–fluid field: Light blue – **reactant fluid**, dark blue – **mixing fluid**, orange – **mild reacting fluid**, red – **flamelet fluid** and green – **product fluid**. The pink iso-contour encloses the reactant fluid, the white iso-contour encloses all OH signal, the black iso-contour encloses the mild reacting fluid, the red iso-contour encloses the flamelet fluid and the mixing fluid is bordered by the pink and white iso-contour.
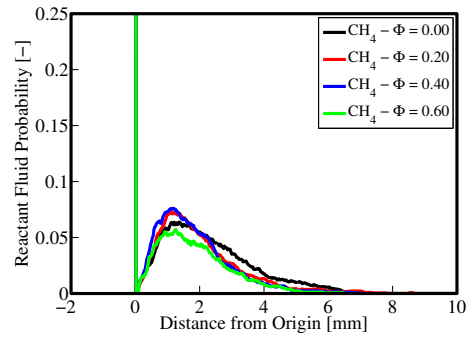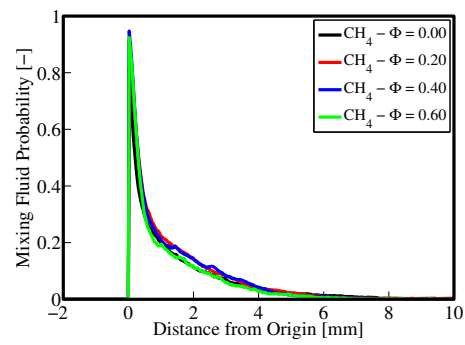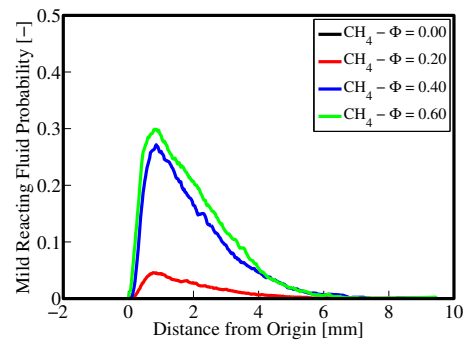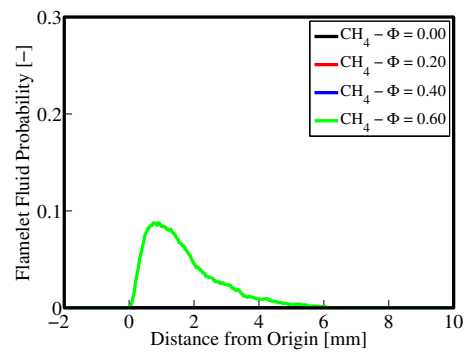
Figure 15: Multi–fluid probability for CH$_4$ at Φ = 0.0, 0.2, 0.4, 0.6: (a) Reactant fluid; (b) Mixing fluid; (c) Mild reacting fluid; (d) Flamelet fluid probability.